The Cryosphere

Novel methods to study sea ice deformation, linear kinematic features and coherent dynamic clusters from imaging remote sensing data

Polona Itkin[1,2]

[1]UiT The Arctic University of Norway, Tromsø, Norway
[2]Norwegian Polar Institute, Tromsø, Norway

Correspondence: Polona Itkin (polona.itkin@npolar.no)

Abstract. Satellite synthetic aperture radar (SAR) data are commonly utilized for calculating sea ice displacements and, consequently, sea ice deformation strain rates. However, strain rate calculations often suffer from a poor signal-to-noise ratio, especially for products with a spatial resolution higher than 1 km. In this study, a new filtering method to strain rate calculations derived from Sentinel-1 SAR image pairs with a spatial resolution of 800 m was applied. Subsequently, a power law to evaluate the deformation rates at decreasing spatial resolutions was employed to assess the quality of the filtered data. Upon positive evaluation of the filtered data, two innovative methods for sea ice deformation assessment were introduced. The first method, named "damage parcel" tracking, involved the combined analysis of displacements and deformation strain rates to monitor divergence and convergence within the sea ice cover. Additionally, a new term to describe the behavior of the winter pack was proposed: "coherent dynamic clusters" (CDCs). CDCs are cohesive clusters of ice plates within the pack ice that move coherently along linear kinematic features (LKFs). The second novel method developed in this study focused on exploring the geometrical properties of these CDCs. Both methods were applied to the January–February collection of Sentinel-1 SAR imagery available during the N-ICE2015 campaign. The damage parcels were continuously tracked over a period of 3 weeks, including a major storm, revealing a slow healing process of existing LKFs. Furthermore, the CDC analysis demonstrated the presence of elongated CDCs with a density ranging from 5 to 20 per 100 km by 100 km, and the shortest distance between LKFs was found to be 5–10 km.

1 Introduction

Sea ice deformation has wide-ranging implications for climate, biology and navigation. For example, the occurrence of leads locally increases the thermodynamic coupling between the atmosphere and ocean, increases light availability for primary production, and aids navigation. On the contrary, the occurrence of pressure ridges increases the surface roughness and dynamical coupling between the atmosphere and ocean, providing a protective habitat for life in the ocean and obstructing navigation. As Arctic ice thins, becomes more seasonal and increases in mobility (Meredith and Schuur, 2019), the processes of sea ice deformation are likely intensifying (Rampal et al., 2009; Olason and Notz, 2014; Itkin et al., 2017). Deformation changes sea ice thickness instantly (Kwok and Cunningham, 2015; Itkin et al., 2018; von Albedyll et al., 2022) and gradually, though preferential melt rates of pressure ridges (e.g., Salganik et al., 2023b), both influencing the state of sea ice, which is critical for accurate sea ice forecasting and projections (Bushuk et al., 2017; Tian et al., 2021). Numerical models and satellite remote sensing products are indispensable tools for monitoring sea ice states and developments. However, existing sea ice rheologies in numerical models, such as those by Hibler (1979), Hunke and Dukowicz (1997), Heorton et al. (2018), and Ólason et al. (2022), do not entirely align with satellite-derived kinematic properties (Hutter et al., 2022). Furthermore, reliable detection of deformed ice and leads (Zakhvatkina et al., 2019; Lohse et al., 2020; Guo et al., 2023), sea ice roughness (Farrell et al., 2020), and sea ice thickness (Ricker et al., 2017) through satellite remote sensing techniques remains

challenging and is plagued by significant uncertainties (Zyg-muntowska et al., 2014; Landy et al., 2020).

Decades of research on sea ice deformation has yielded significant progress, leading to a better understanding of its multi-fractal nature, as extensively documented in the literature (Erlingsson, 1988; Schulson, 2004; Marsan et al., 2004; Hutchings et al., 2011; Itkin et al., 2017; Oikkonen et al., 2017). This body of knowledge reveals that various features, such as small cracks approximately 1 m wide; ridges with a width of 10 m; leads spanning 100 m or more; and even complex systems of linear kinematic features (LKFs; first described by Kwok, 2001), measuring 1 km or wider, exhibit similar characteristics in both space and time. This self-similarity extends not only to their shapes but also to the strain rates within these fractures. Such patterns can be described using scaling laws, enabling the measurement of deformation at a specific spatial or temporal resolution and facilitating comparisons between different datasets, regions and seasons. These comparisons, in turn, are instrumental in evaluating numerical models (Rampal et al., 2019; Hutter et al., 2022). Furthermore, it has been observed that sea ice fractures of various spatial scales tend to occur at typical intersection angles (Erlingsson, 1988; Hutter et al., 2022; Ringeisen et al., 2023). These fractures align along the Mohr–Coulomb failure lines, dividing the ice surface into distinct, parallelogram-shaped plates that move relative to one another, much like tectonic plates on a planet (Erlingsson, 1988; Schulson, 2004; Dansereau et al., 2019). In this paper the cohesive clusters of these plates are called coherent dynamic clusters (CDCs) – a name that describes the transient nature of their motion along the fractures. CDCs can be described by size and shape parameters, offering a novel option for sea ice deformation characterization. Motion of CDCs along the fractures can persist for several days (Coon et al., 2007; Graham et al., 2019), although strain rates typically cycle between divergence and convergence over the course of a weather event (Graham et al., 2019). The collision and sliding along these fractures cause damage to the CDC edges, manifesting as leads and ridges. Over time, these features can consolidate by healing at low temperatures (Oikkonen et al., 2016) or through the injection of freshwater from snowmelt in the spring (Salganik et al., 2023a). As a result, the consolidated ridges and refrozen leads in CDCs reflect past deformation events. At any given moment, these CDCs may separate along newly formed fractures in either undamaged or previously damaged ice. Ridges and leads can also reactivate (Oikkonen et al., 2017), as any ice damage presents a weak point in the ice cover that can persist over seasonal timescales. Thus, damage should be considered an additional parameter – alongside thickness and roughness – emerging from sea ice deformation. Research has shown that incorporating damage into numerical models of sea ice (Girard et al., 2011) can enhance the representation of deformation and improve sea ice thickness distribution in modeling efforts (e.g., Ólason et al., 2022).

Although deformation can be estimated from sequential buoy positions (Rampal et al., 2009; Hutchings et al., 2011; Itkin et al., 2017) or obtaining displacements by comparing images, such as those from X-band ship radar (Oikkonen et al., 2017), much of the progress in this field is reliant on a vast volume of C-band satellite synthetic aperture radar (SAR) data, including data from the RADARSAT program of the Canadian Space Agency and Sentinel-1 mission of the European Space Agency. Sea ice displacements can be determined from sequential SAR images using feature or pattern tracking algorithms (Hollands and Dierking, 2011; Komarov and Barber, 2014; Korosov and Rampal, 2017), which are then utilized to calculate strain rates (Kwok, 1998; Kwok and Cunningham, 2015; von Albedyll et al., 2021). Specifically, the RADARSAT Geophysical Processor System (RGPS) (Kwok, 1998) has been instrumental in deriving properties such as scaling laws in spatio-temporal distribution (Marsan et al., 2004; Bouillon and Rampal, 2015; Rampal et al., 2019) and patterns in LKFs (Hutter et al., 2022). However, the spatial resolution of deformation estimated from SAR has been constrained to be coarser than 1 km by the signal-to-noise ratio (von Albedyll et al., 2021; Ringeisen et al., 2023).

The aim of this paper is to explore the potential use of Sentinel-1 SAR data at higher spatial resolutions to investigate sea ice deformation properties. This paper utilized sea ice deformation data and findings from the N-ICE2015 expedition conducted in January and February 2015 in the pack ice north of Svalbard, as reported by Granskog et al. (2018), Itkin et al. (2017), Oikkonen et al. (2017) and Graham et al. (2019). The methodology involved comparing the power law of SAR-derived strain rates with other N-ICE2015 data. In the next phase, this study examined whether SAR data could be employed to track damage along LKFs between temporally separate weather events. Finally, the paper explored the possibility of detecting CDCs.

2 Data

The N-ICE2015 expedition (Granskog et al., 2018), conducted aboard RV *Lance* as it drifted freely with the pack ice (Fig. 1), provided an exceptional dataset on sea ice deformation. This expedition marked a historic moment as it enabled simultaneous high-resolution deformation observations from GPS buoys (Itkin et al., 2015), ship radar (Haapala et al., 2017) and satellite SAR. In this paper, data from the winter leg (leg 1), spanning mid-January to mid-February, were utilized. During this period, the pack ice in the N-ICE2015 region consisted mainly of second-year ice to the north and northwest of RV *Lance*, while first-year ice was prevalent in the south and southeast (Itkin et al., 2017). Over the course of the month analyzed in this study, the distance between the ship and the ice edge decreased from 200 to 50 km. Additionally, several storms, which induced significant sea ice
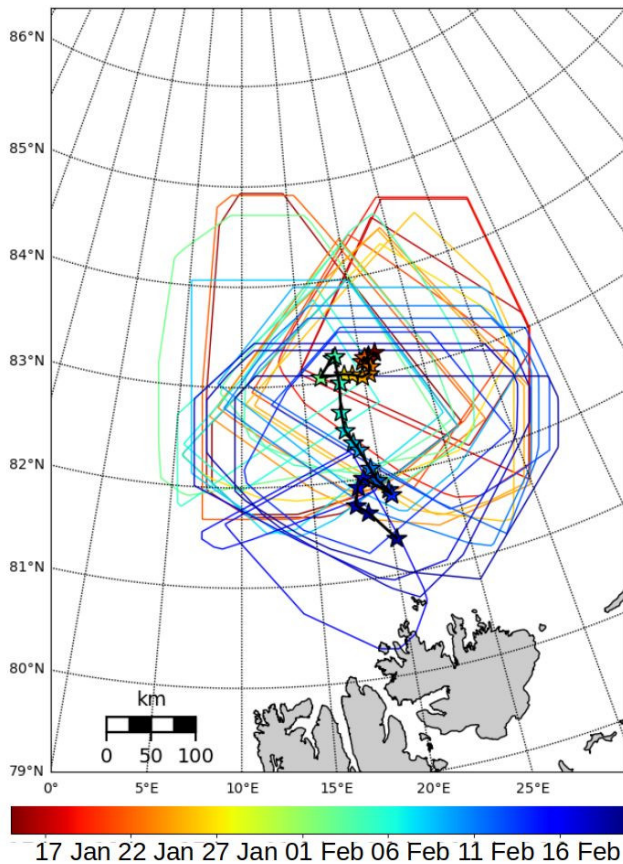
Figure 1. The N-ICE2015 RV *Lance*'s daily positions (stars) from 15 January to 18 February. The ship drifted southwards, with the colors of the stars increasing with time. The frames show the total coverage of the SAR sea ice deformation dataset for each day in the radius of 200 km from RV *Lance*. After 18 February, the ship reached the ice edge and was relocated back towards 83° N, 25° E.

deformation, passed over the pack ice during this time frame (Graham et al., 2019). For a comprehensive understanding of sea ice deformation during N-ICE2015, readers are encouraged to refer to the works of Itkin et al. (2017) and Oikkonen et al. (2017). Further details regarding the expedition's atmosphere–ice–ocean interactions can be found in the summary provided by Graham et al. (2019).

Central to this paper are the 145 Sentinel-1A synthetic aperture radar (SAR) images obtained from the CREODIAS 2.0 server (cre, 2023), tracking the same sea ice area during the N-ICE2015 expedition north of Svalbard from 15 January to 18 February 2015. An additional 49 images were downloaded to extend the CDC analysis until 27 February. These images were among the initial operational data from the Sentinel-1A mission. All the satellite images were acquired in extra-wide-swath mode, the typical mode activated over sea ice, providing level-1 ground-range-detected (GRD) images with a 410 km wide swath and a pixel size of 40 m by 40 m. The advantageous high-latitude location of the expedi-

tion allowed for data collection in two temporal clusters of the polar-orbiting satellite: the ascending orbit in the early morning (05:00 to 08:00 UTC) and the descending orbit in the afternoon (13:00 to 16:00 UTC). However, there were several episodes during the month when GRD data were unavailable, notably between 27 January and 3 February.

The ship radar data from N-ICE2015 were obtained through the digitizing unit of the navigational X-band radar installed on RV *Lance* (Karvonen, 2016; Haapala et al., 2017). The radar antenna, positioned at a considerable height on the ship's mast, offered a range of 15 km with minimal mast shading and a spatial resolution of 12.5 m. For this study, the processed total deformation rates derived from daily radar image pairs, as processed by Oikkonen et al. (2017), were utilized. To align with the temporal coverage of the Sentinel-1 data, the week between 27 January and 3 February was excluded for comparative analysis.

During the N-ICE2015 expedition, an extensive array of GPS buoys was deployed in two concentric rings around RV *Lance*, transmitting data at hourly and 3-hourly intervals (Itkin et al., 2015). For this study, only the inner ring, with a diameter of approximately 20 km and comprising 11 buoys, was analyzed. The external ring of the buoys was incomplete towards the north and thus excluded from the analysis.

3   Methods

All datasets were processed into spatially distributed points, capturing known displacements at defined, ideally daily time steps. The highest spatial scales of the ship radar and buoy data were determined based on signal-to-noise ratios, following the approach suggested by Hutchings et al. (2012). For more detailed information on the processing of ship radar and buoy data, readers can refer to Oikkonen et al. (2017) and Itkin et al. (2017).

Sea ice displacements from SAR image pairs were estimated using a sequence of feature tracking (FT) and pattern matching (PM) methods developed by Korosov and Rampal (2017). While not radiometrically calibrated, each image was multi-looked, averaging radar intensity values over an 80 m by 80 m area. This process helped mitigate speckle noise that could introduce errors in the geographical positioning of features or patterns in the image. In the subsequent step, the FT method provided the initial estimate of displacements on an irregular grid for each SAR image pair. These initial estimates were used to narrow the local search radius, improving the computational efficiency of the subsequent PM method applied to the same image pair. For PM, a regular orthogonal grid with points separated by 800 m (10 pixels) was seeded. Using a regular grid was advantageous for sea ice deformation calculations as it provided the foundation for a triangulation mesh with elements of comparable length scales. In the PM method, image sub-samples (templates) measuring 3.2 km by 3.2 km (45 by 45 pixels) were matched based
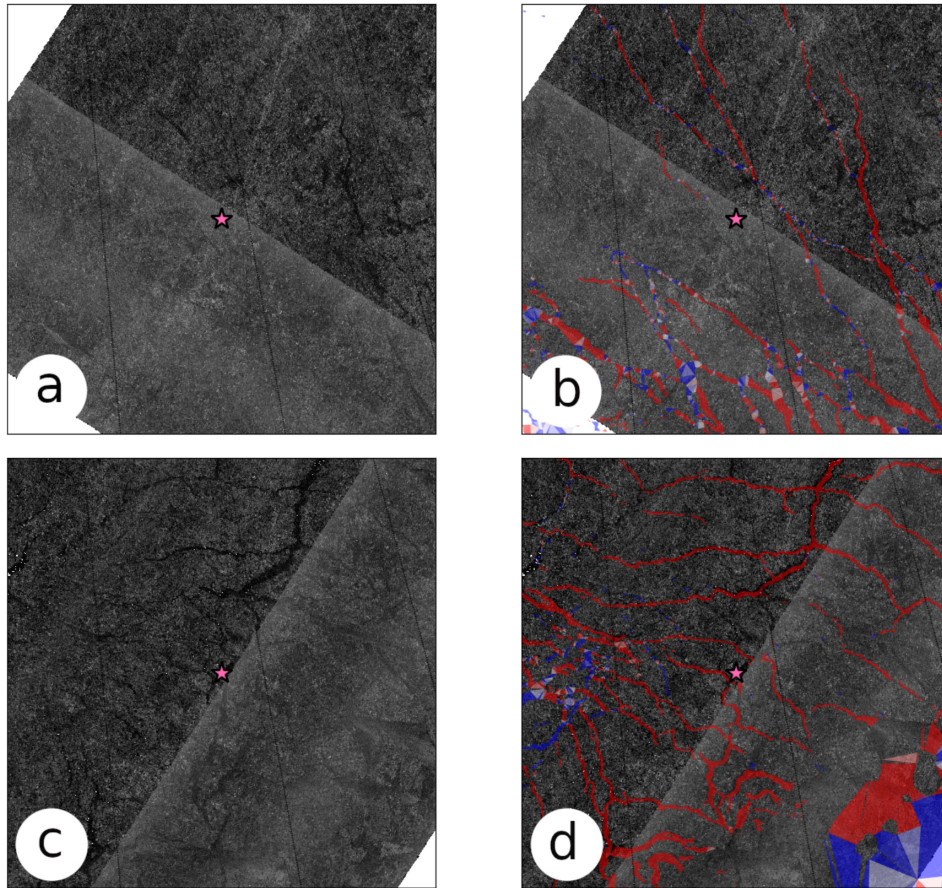
Figure 2. Second SAR image in the pair **(a, c)** overlaid by calculated deformation from the image pair **(b, d)** for 25 January **(a, b)** and 9 February 2015 **(c, d)**. The sizes of the frames are 200 km by 200 km. The location of RV *Lance* is represented by a pink star in the centers of the frames.

on mean displacements from FT. Maximum cross-correlation (MCC) with rotation was utilized to estimate displacements, and a threshold value of the Hessian matrix of the MCC was empirically determined and employed as a quality control measure. Displacements with values lower than this threshold were discarded, effectively removing geometrical artifacts such as image edges.

The estimation of sea ice deformation from sea ice displacements followed the same method for all three datasets. The displacements were converted into average velocities by dividing them by the time differences between the recorded positions. Initially, the origin displacement location points were triangulated using Delaunay triangulation, where triangles with one of the angles sharper than 15° were discarded. Sea ice deformation was then estimated using the commonly used line integrals of Green's theorem (Marsan et al., 2004; Hutchings and Hibler III, 2008). Shear and divergence were estimated from spatial derivatives of velocities: u_x, u_y, v_x and v_y. Here, u_x is defined as

$$u_x = \frac{1}{A}\Sigma_{i=1}^{n}(u_{i+1} + u_i)(y_{i+1} - y_i), \tag{1}$$

where A is the area of a triangle, i is the index of a corner of a triangle, $n = 3$ and $n + 1 = 1$. The other derivatives are defined in a similar way. The shear ϵ_{SHR}, divergence ϵ_{DIV} and total deformation rate ϵ_{TOT} are then defined as

$$\epsilon_{\text{SHR}} = \sqrt{(u_x - v_y)^2 + (u_y + v_x)^2}, \tag{2}$$

$$\epsilon_{\text{DIV}} = u_x + v_y, \tag{3}$$

$$\epsilon_{\text{TOT}} = \sqrt{\epsilon_{\text{DIV}}^2 + \epsilon_{\text{SHR}}^2}. \tag{4}$$

3.1 Additional SAR sea ice deformation processing

In this study, an 800 m distance between grid points was chosen as the highest resolution for the SAR data analysis. Although a higher resolution was technically feasible, it would not be advantageous for the comparison with the ship radar and buoy data. The 800 m grid spacing aligns with one of the shorter length scales of ship radar data and is wider than most of the leads and linear kinematic features (LKFs) observed during N-ICE2015, as reported by Graham et al. (2019). Opting for a shorter distance would have limited the sampling of

the shortest distance (λ) over these fracture zones, compromising the accuracy of the power law scaling analysis.

The accuracy of the data, denoted as σ_x, can be estimated as 80 m, representing the lowest detectable displacement. Following the signal-to-noise ratio formulation by Hutchings et al. (2012), sea ice deformation calculations become reasonably noise-free when $A \gg 8n^2\sigma_x^2$, where A is the area of the polygon with n number of nodes (three nodes for a triangle). If $\lambda = \sqrt{A}$, this condition is satisfied only when $\lambda \gg 679$ m, for example, for values that are an order of magnitude larger, such as 5–10 km. Consequently, sea ice deformation calculations at shorter length scales are not reliable. This limitation is clearly visible in Fig. 3a. The noise arises from undetectable displacements shorter than the pixel size (σ_x) of the SAR images. These short displacements are extremely low or even close to zero. The residual deformation resulting from these displacements accumulates in artifacts with rhomboid shapes. These shapes appear due to the step function in the sea ice displacement algorithm: the value of a displacement can only increase by σ_x. These increases occur perpendicular and parallel to the template rotation in PM, creating a rhomboid pattern that becomes denser in regions where the velocity gradients are larger. It is crucial to note that this pattern should not be confused with similarly shaped fractures following Mohr–Coulomb failure lines in linear kinematic features (LKFs) (Erlingsson, 1988; Schulson, 2004; Dansereau et al., 2019). Realistic features, however, stand out as locations with a stronger signal, correctly spatially confined to leads (see Fig. 2). Calculating deformation at a coarser spatial resolution, which would smooth the rhomboid artifacts, would inevitably lead to the loss of information about the location of deforming sea ice. As demonstrated by Korosov and Rampal (2017) using the example of coastline locations, the sea ice displacement algorithm exhibited a spatial accuracy of approximately 200 m, significantly higher than the 800 m resolution used in this study.

To examine if the deformation values in those features were also realistic, they were isolated by applying a detection limit (DL) defined as

$$\text{DL} = nk\sigma_x^2/(2A\text{d}t), \qquad (5)$$

where k is the scaling coefficient of σ_x, and $\text{d}t$ is the time difference between the images in the image pair. The rhomboid artifacts have values right at the DL for $k = 1$ and can be efficiently removed by threshold DL for, e.g., $k = 1.3$. In this study this increases the σ_x by 30 % from 80 m to approximately 120 m.

In addition to the signal-to-noise ratio issues in the displacement data, another source of error in the deformation estimates by line integrals stems from the orientation of the LKFs concerning the triangle boundaries. Equation (1) assumes a homogeneous velocity gradient along the boundary, a condition often violated in triangles – polygons with just three nodes, where an LKF can cross its boundary under any angle. This "boundary definition error" is a well-known problem (Lindsay and Stern, 2003; Bouillon and Rampal, 2015) that can lead to spurious opening and closing along the LKFs. While this problem can be mitigated by isotropic smoothing (Lindsay and Stern, 2003), Bouillon and Rampal (2015) suggested a directional filtering of deformation values of triangles specifically along the LKFs. Such anisotropic smoother, here called the LKF filter (LKFF), follows the direction of the LKF and preserves the accurate information of the deformation localization. LKFF was defined by the size of the kernel, the number of boundaries crossed in each direction and its minimal size. LKFF was applied to the data previously filtered by DL. The kernel size suggested by Bouillon and Rampal (2015) was three for a dataset with 10 km grid spacing. In this study, the spacing is much shorter (800 m), and the smallest possible kernel of one boundary crossing was used. For a single LKF this resulted in an LKFF size of three triangles, while for a complex case of LKF crossing, the kernel size may be larger. Only deformation features with at least one entire kernel size were considered, while the others were removed. This eliminated the rhomboid artifacts that persisted after the DL filtering, owing to accumulated noise in the "corners" of the rhomboids, where two directions of the step function crossed. LKFF averages out the spurious switching between divergence and convergence from one triangle to the next (compare Fig. 3a and b) and reduces the deformation values. As triangles along the LKFs may have varying sizes, the averages were weighted by the triangle area.

An overview of the methods for SAR sea ice deformation used in this paper is given in Fig. 3.

Each SAR image pair had a restricted spatial extent and occasionally did not cover the entire sea ice surface. To expand the data coverage, several surrounding image pairs were processed for deformation and then tiled together. Since the time difference between the pairs varied, different DL values were correspondingly applied. Figures 2 and 3 already display such a tiled product.

To facilitate comparison, SAR-derived deformation values were coarse-grained from the original 800 m resolution into logarithmically spaced λ, similar to the other two data sources. The minimum spatial coverage of any coarse-level triangle by fine triangles was set at 10 %, and the assigned values were means weighted by the spatial coverage. Triangles with spatial coverage below this threshold were discarded.

3.2 Comparison of the N-ICE2015 strain rates

To assess whether the sea ice deformation derived from SAR by the methods described in the previous section was realistic, SAR-derived data were compared to the ship radar and buoy data. Unfortunately, the ship radar and buoy deformation data used in this study were just collections of values. The ship radar deformation maps calculated by Oikkonen
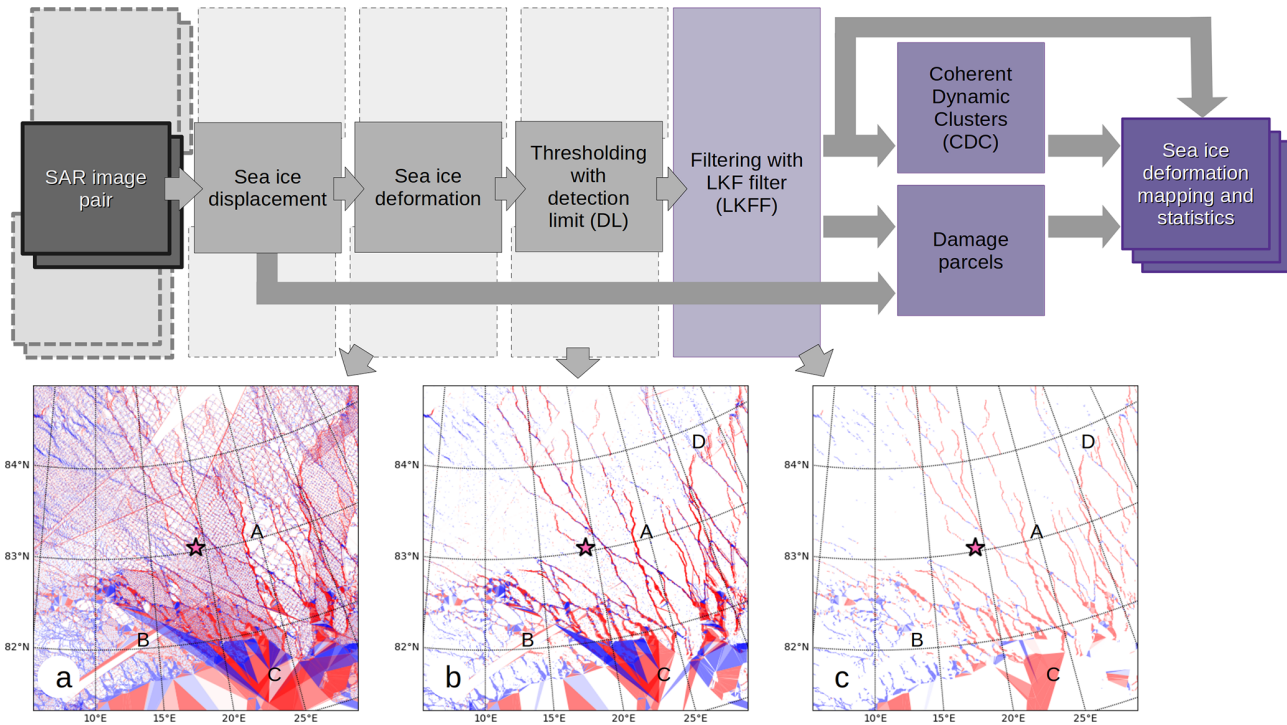
Figure 3. Flow chart of the SAR processing methods for sea ice deformation applied in this paper. SAR image pair in the dark gray box is the input information. The light gray boxes show the intermediate steps with calculations of the sea ice displacements, deformation, DL thresholding and LKF filtering. The purple boxes show the outputs and each next level with an increase in color shading density. The secondary rows of the first four squares depict tiling. The LKFF products merge the tiles and span the entire region. The bottom of the figure shows examples of the SAR deformation processing: **(a)** original, **(b)** DL filtered and **(c)** LKF filtered (LKFF) for a mosaic of SAR image pairs for 25 January 2015. The sizes of the frames are 400 km by 400 km. The location of RV *Lance* is represented by a pink star in the centers of the frames. The step-wise evolution of specific cases is marked by capital letters: A – removal of rhomboids, B – removal of image edges, C – persisting problems in the marginal ice zone (MIZ) and D – merging of the tiled information (disappearing shadow effect).

et al. (2017) were not geolocated or stored, and the spatial scales λ of the buoy array are too coarse to compare directly to the ship radar values. To enable comparison between all three datasets, the power laws across all available λ for daily total deformation ϵ_{TOT} were estimated. Sea ice deformation is known to be a highly localized process, where mean ϵ_{TOT} ($\overline{\epsilon}_{\text{TOT}}$) follows the power law with respect to λ: $\overline{\epsilon}_{\text{TOT}} = \alpha \lambda^{\beta}$ (Marsan et al., 2004), where α is the interception at $\lambda = 1$, and β is the slope of the power law. ϵ_{TOT} also depends on the temporal scale at which they were measured – there is also a power law at an increasing temporal scale (Oikkonen et al., 2017). To account for this, the daily resolution of the buoy and ship radar data was strictly observed, while for the SAR image pairs more lenient criteria were necessary, and only the temporal difference between 22 and 26 h was used for this part of the analysis. The ship radar and buoy data were also filtered by DL values determined by the SAR data. Because the data were collected over the same region and over the same time window, the same magnitude of sea ice deformation was expected. This allowed for a comparison of α in addition to typically used β (Marsan et al., 2004; Bouillon and Rampal, 2015; Itkin et al., 2017; Oikkonen et al., 2017).

The confidence envelope of the power law was estimated as a two-tailed t test as in Itkin et al. (2017).

3.3 Damage parcels

The spatially distributed sea ice deformation values obtained in the previous section were used to classify the sea ice cover into damaged (deformed) and undamaged (undeformed) ice. For such classification a zero threshold of total deformation was used. Afterwards, divergence values were used to further classify damaged ice into predominantly ridged (convergence) and predominant lead ice formation (divergence). The advantage of this two-stage classification was that, first, the total deformation was used to give a relatively reliable division between undamaged and damaged ice. Although the LKFF removed some of the spurious divergence, the second-stage classification was less certain.

Such classification was tracked for a sequence of time steps (SAR image pairs). The second SAR scene in each pair was always the first scene in the following pair. A strict daily time difference between the image pairs was not observed. The tracking was not done for individual triangles because

of frequent distortion of the triangles beyond the 15° minimal angle criteria. To avoid numerically costly re-meshing, a simple approach with "ice parcels" was used instead. Ice parcels can be used in applications where mass preservation is not critical (e.g., Liston et al., 2020; Horvath et al., 2023). Displacements calculated as input to the sea ice deformation calculations were used to update the location of damaged ice parcels between the time steps.

At the beginning of the damage tracking procedure, the entire area is seeded by equally spaced undamaged parcels. In subsequent steps, each parcel is tracked, and its value of damage, convergence or divergence accumulates by the deformation value found within the search radius. At the same time its location is updated. This procedure is repeated for all time steps. After the last time step the accumulated values of damage are used to classify each parcel into the predominately leads, ridged ice, mixed class and undamaged ice categories. Figure 4 gives an overview of the damage parcel tracking method. The spatial resolution of the damage parcel product in this study was 800 m, limited by the resolution of the input data (800 m spacing of the sea ice deformation and sea ice displacements) and by the search radius within which the input data are attributed to each parcel (also 800 m). If multiple triangle centroids fell within the search radius, the mean value was attributed to the parcel. If no value was found, the parcel disappeared. New parcels were added in the empty areas between the parcels, i.e., wide leads. An early version of this method was used by Guo et al. (2022) for the same study area as in this paper.

3.4 CDCs and LKFs

As defined in the Introduction, CDCs are clusters of ice plates, containing damaged or undamaged ice, which at a given moment in time move coherently within each other and differentially with respect to the other CDCs that are disconnected from them by fractures like LKFs. CDCs are transient features that only describe the state of the pack ice at a certain moment in time. A statistical description of the geometrical characteristics of CDCs and LKFs can therefore be used to evaluate the state of ice over time. Such a statistical description suggested here was determined by using the location information of the deformation calculations. The triangle nodes filtered by LKFF were used to calculate polygons in computational geometry operations, such as polygon union, distance buffering, difference (removed intersection) and removal of polygon holes, as shown in Fig. 5. The resulting polygons were classified into CDCs and LKFs, and the following characteristics were determined at each time step:

- *CDC size* and *CDC density* are measured as the area of the CDC (km^2) and number of CDCs per total area A (km^{-2}). At time steps with very low sea ice deformation, the entire region may be divided into just one or a few large CDCs, while at time steps with strong deformation, it may be divided into many small CDCs. CDC size is a variable more appropriate for mapping, while time series regional comparisons may be better achieved by comparing CDC density.

- *CDC circularity* is a measure of the roundness and compactness of CDCs. It is determined by the isoperimetric quotient – the ratio of CDC area A to the circle having the same perimeter, $\frac{4\pi A}{p^2}$, where p is the convex hull perimeter of the CDC polygon. Completely circular CDC scores have a value of 1, while smaller values are typical of less compact shapes (e.g., the square score corresponds to 0.75). The convex hull perimeter is used instead of the CDE perimeter due to its sensitivity to overall elongation and the angularity of the shape, while being insensitive to the properties that are indicative of fragmentation. To compare the CDC shapes to the summer floe shape values (e.g., Hwang and Wang, 2022), the more frequently used *CDC roundness* was calculated. Roundness is less sensitive to "squareness" as it is a simple ratio between the max and min diameter of CDC (see next point), with values close to 1 for circular CDE.

- *CDC complexity* is a measure of fragmentation, and it is determined by a ratio between the CDC perimeter and its mean diameter. The mean diameter is the average of the min and max diameter estimated from the min and max radius. First, the centroid of the CDC is calculated. The min and max radii are then the shortest and the longest distance to the CDC boundary. CDC complexity has a theoretical value close to 2 for simple elongated polygons (practically a very slim rectangle). Typical values span 4 for parallelograms, expected for sea ice, and 7 for complex polygons with meandering boundaries. The latter is typical of CDCs where the LKFF likely fails to detect small deformation and correctly divide such a deformation into several smaller CDCs. Large CDC complexity is therefore a measure of error of the method.

- *LKF fraction* is the LKF area per total area. It is determined by two separate methods: (1) by summing the area of LKF-filtered triangles (min LKF fraction) and (2) by summing the area not covered by CDCs (max LKF fraction). The first method is more conservative than the latter, while the latter gives another measure of undetected deforming ice parcels.

- The *distance between LKFs* is estimated from the min and max CDC diameter used to estimate CDC complexity (see above). Based on the diameters, the min and max distances are estimated.

The vector operations required empirical tuning of parameters such as buffer distances and minimal sizes (Table 1).
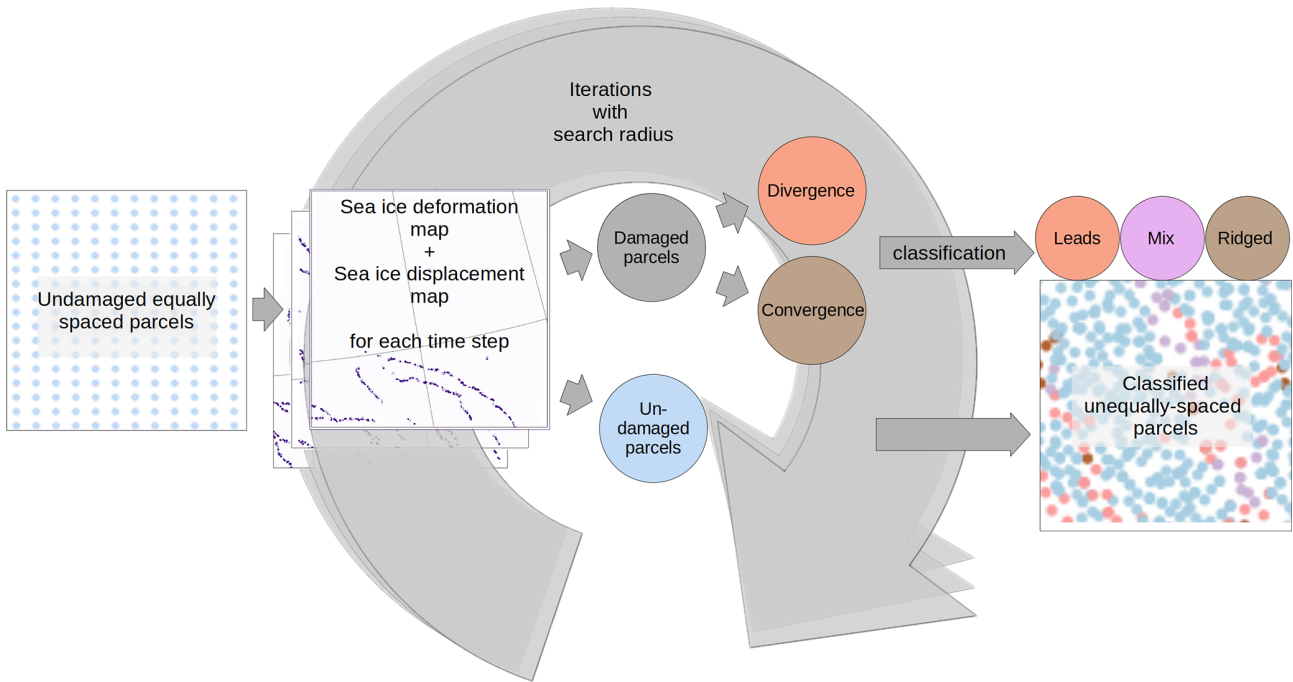
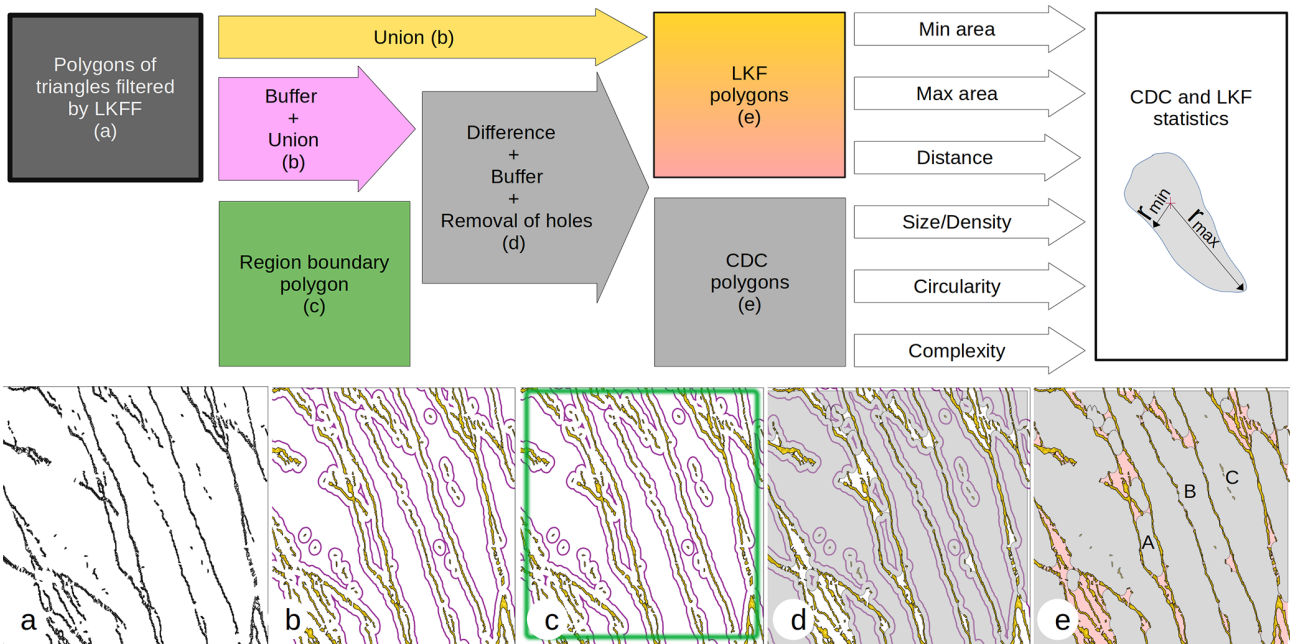**Figure 4.** Flow chart of the damage parcel mapping applied in this paper.

Figure 5. Flow chart of the CDC and LKF polygon operations and sub-figures showing examples of the sequential steps: **(a)** union of LKFF triangles, **(b)** 4 km buffers around the triangles and their union, **(c)** regional frame that supplies part of the outer boundary to some of the polygons, **(d)** difference between the region and the LKF polygons with removal of internal polygons (holes) and reclamation of the buffered area, and **(e)** final CDC and LKF polygons. The step-wise evolution of specific cases is marked by capital letters: A – small and initially not separated CDC, B – initially partially disconnected boundary of a large CDC, and C – removed holes caused by under-detected LKF. The illustration of a CDC in the box on the top right shows the centroid (+) and min and max radii of a polygon.

The buffer distance was used to merge disconnected polygons of the same LKFs in cases where parts of the polygon were not detected. Later, the same buffer was added to expand CDC polygons back towards the LKFs. The maximum LKF triangle size removed triangles in the MIZ, where CDC and LKF detection is not possible. The minimal size of the CDC limited the unrealistic fragmentation of ice cover into small CDCs.

4   Results and discussion

4.1   Comparison of the N-ICE2015 strain rates

The spatial power law in ϵ_{TOT} was initially compared for the data obtained from the N-ICE2015 ship radar and buoys (Fig. 6a). For the complete dataset, the power laws exhibited similar intercepts, α (20.15 and 15.91), and slopes, β (-0.6 and -0.69). Both power laws cover different spatial scales (λ): the ship radar data span 200 m to 3 km, while the buoy data span 3 to 8 km. Before comparing them to the filtered SAR-derived data, the ship radar and buoy data needed to be filtered in a similar manner (Fig. 6b). Values below DL, estimated from mean DL values in SAR data, were removed from the ship radar and buoy data. This filtering increased α for the ship radar to 24.61 and decreased β to -0.7. For the buoys, the removal of values below DL led to a counterintuitive slight decrease in α to 15.24. Note that the power law for buoy data is based on mean values for only three λ values, resulting in a wider confidence envelope. LKFF filtering of the ship radar and buoy data was not feasible, as described in the Methods section under "Comparison of the N-ICE2015 strain rates".

Figure 6b also shows the power laws for the SAR-derived data. The unfiltered data had a large number of low values that decreased the β of the power law. DL filtering successfully removed these values, increased α from 4.79 to 14.63 and decreased β from -0.14 to -0.59. To construct the power law, only means for λ shorter than 10 km were used. This is revisited later in this section. The LKFF further increased α to 18.73 and decreased β to -0.73. The power law from LKF-filtered SAR data corresponded well to the ship radar and buoy data power laws within their confidence envelopes. The temporal resolution is not strictly daily for all datasets, and the area is not strictly the same, so some differences in power law are expected. Thus, the high deformation rates detected by SAR were reliable, and LKFF SAR-derived deformation was useful at short λ.

A further confirmation that the LKFF SAR estimates were reliable was the conversion of the ϵ_{TOT} values in Fig. 6a and b to mean total displacements ($\overline{\sigma_x}$). This was done by a simple rearrangement of Eq. (5), used to estimate DL, such that $\overline{\sigma_x} = \sqrt{\frac{\epsilon_{\mathrm{TOT}}(2A\mathrm{d}t)}{3}}$. The displacements are more intuitive than strain rates and are comparable to any other distances over space, such as ridge and lead widths or even sea ice thickness. A total displacement of 100 m can, for example, mean 70 m widening of a lead with 30 m of shearing. Figure 6c shows that $\overline{\sigma_x}$ at 1 km was about 200 m for all three datasets. This corresponded to a triangle with sides of about 1 km experiencing a sum of divergence and shear of approximately 200 m. If extrapolated to 100 m, $\overline{\sigma_x}$ was approximately 50 m. Both 1 km and 100 m values were within the expected ranges for medium- and small-size leads. At 1 m, $\overline{\sigma_x}$ for DL-filtered data was in the range of 3–4 m, and for the non-filtered data for ship radar and buoy data, it was in the range of 1–2 m. The latter values are comparable to the mean sea ice thickness measured in the pack ice at N-ICE2015 (Rösel et al., 2018). These values correspond to the expected theoretical values of $\overline{\sigma_x}$ (Weiss, 2017). A practical use of recalculating the strain rates to total displacement is also in observations (e.g., Nicolaus et al., 2022; Parno et al., 2022) or simulation design. To resolve, for example, 100 m displacements (small leads), 10 m displacements (large ridges) or 1 m displacements (cracks), accurate measurements at 200, 30 or 1 m resolution at daily scale are required.

In addition to the power law of $\overline{\epsilon_{\mathrm{TOT}}}$, other values are also scaled with λ (Fig. 6). For example, the DL values followed a power law which suggested that only at $\lambda \gg 10$ km did no ϵ_{TOT} values fall below DL anymore. This matched the noise-free estimates following Hutchings et al. (2012) (see the Methods section). Finally, another sharp limit stood out in the data: the maximum values of ϵ_{TOT} and σ_x follow a power law with a matching slope to the DL power law but with an interception higher by approximately 2 orders of magnitude. At 1 km, the maximum ϵ_{TOT} and σ_x values were approximately $40\,1 \times 10^{-6}\,\mathrm{s}^{-1}$ and 2 km, respectively, for all three datasets. There is no natural explanation as to why σ_x should be limited to values below 2 km, as Arctic leads and polynyas can be much wider than that (Wernecke and Kaleschke, 2015). This hard limit was a consequence of the 15° angle limit in the triangles used for strain rate calculations and another manifestation of the deficiency of estimates by line integrals (Green's theorem) (Marsan et al., 2004; Hutchings and Hibler III, 2008) in simple polygons like triangles. The 15° rule is often violated in fast-deforming features that have relative displacements beyond 2 km over a given time step.

The filtering of SAR-derived deformation resulted in widespread missing values (Fig. 7). In the coarse-graining of λ, at least 10 % of the area was required to have valid data. This means that as λ became coarser, data had an increased fraction of missing values. The problem was demonstrated on maps in Fig. 7 with an example from 25 January. The individual LKFs remained visible up to λ 4.5 km. With λ 9.6 km, the lines were discontinued, and only triangles containing either very wide or multiple LKFs at shorter λ remained. The few remaining values at λ larger than 10 km were relatively high, and their means did not follow the power law (Fig. 6b). Such a "breaking point" between 5 and 10 km has previously been detected in the comparison of the hourly buoy and ship radar data from N-ICE2015 (Oikkonen et al., 2017). The reason

Table 1. Empirical parameters used in geometry operations to derive LKF and CDC polygons.

Name	Description	Value in this paper
Buffer	Max distance (in m) between two nodes of different triangles to get connected into the same LKF. This is a circular buffer, and there is a trade-off between a desirable connection over parts of the same partly undetected LKF and undesirable connection across the breadth of two separate but close-by LKFs.	4000
LKF max triangle	Maximum area of LKF triangle to be taken into account – here the area of 12 right-angled triangles. This will exclude large triangles in the MIZ.	3.84×10^6
Min area	Min area of the CDC and small CDC (in m^2).	1×10^7
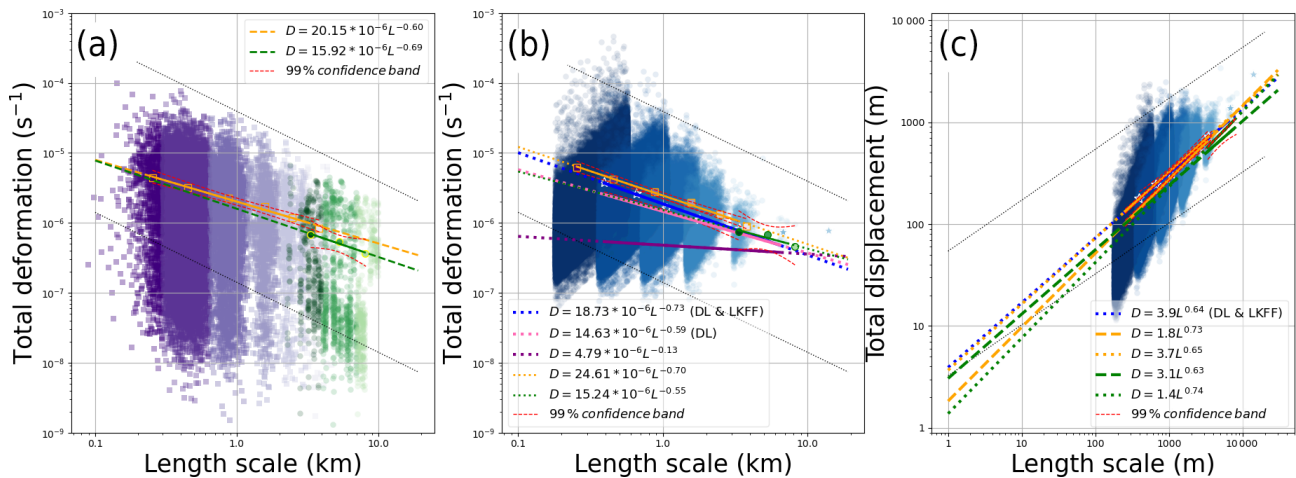
Figure 6. Power law for the spatial scales of ship-radar-, buoy- and SAR-derived sea ice deformation calculations: **(a)** original values from ship radar (purple shades with means for logarithmically distributed length classes as orange rectangles) and buoys (green shades with means as circles), SAR-derived deformation (blue shades with stars as means) and DL-filtered ship radar and buoy values, and **(c)** total displacements. The total displacements in panel **(c)** have a matching y axis, but the x axis is stretched to the left to show extrapolation of the power law to 1 m scale displacements. The power laws are fitted to the length-scale class mean. Power laws with long dashed lines include all data, and power laws with short dashed lines only include the DL-filtered data. DL and max values are shown with dashed thin black lines in all plots.

for this may be because of the under-detection of the self-similarity of sea ice deformation by the N-ICE2015 data. None of the datasets have a spatial resolution high enough to resolve the cracks. Likewise, all have a spatial extent limited to the local ice cover with a radius of 10 to 200 km, insufficient to resolve the pan-Arctic systems of LKFs. LKFs remain the only spatial feature which all three datasets could resolve. Figure 6 shows how removing low values increases the power law slope. Adding values from unresolved cracks would, therefore, decrease it. Some datasets that could be used to measure deformation cracks (resolution 1 m) already exist (Clemens-Sewall et al., 2022) but have very poor temporal resolution (weekly). On the contrary, adding the spatial extent should decrease the values at large λ to prevent the power law from breaking. SAR data are already available at the pan-Arctic scale (Kwok, 1998; Howell et al., 2022), but the resolution used in this study produces data volumes that are challenging and will be the subject of future studies.

4.2 Damage parcels

Sea ice damage parcels were tracked for 19 d, starting from 15 January to 3 February (see Fig. 8). Daily image pairs were available from 15 January to 27 January. Subsequently, deformation was successfully calculated for an image pair from 27 January to 3 February, allowing for the continuation of parcel tracking. During the 8 d period of missing data, from 27 January to 3 February, the conditions were relatively quiescent in terms of weather and sea ice motion (Itkin et al., 2017; Graham et al., 2019). Afterward, between 3 February and 5 February, SAR data were available, but the ice cover experienced a major storm (Graham et al., 2019), leading to unusually strong deformation (Itkin et al., 2017; Graham et al., 2019), which prevented further parcel tracking.

The parcel map (Fig. 8) illustrates a network of ice parcels primarily experiencing divergence within LKFs. This pattern persisted throughout the entire period, with the same parcels
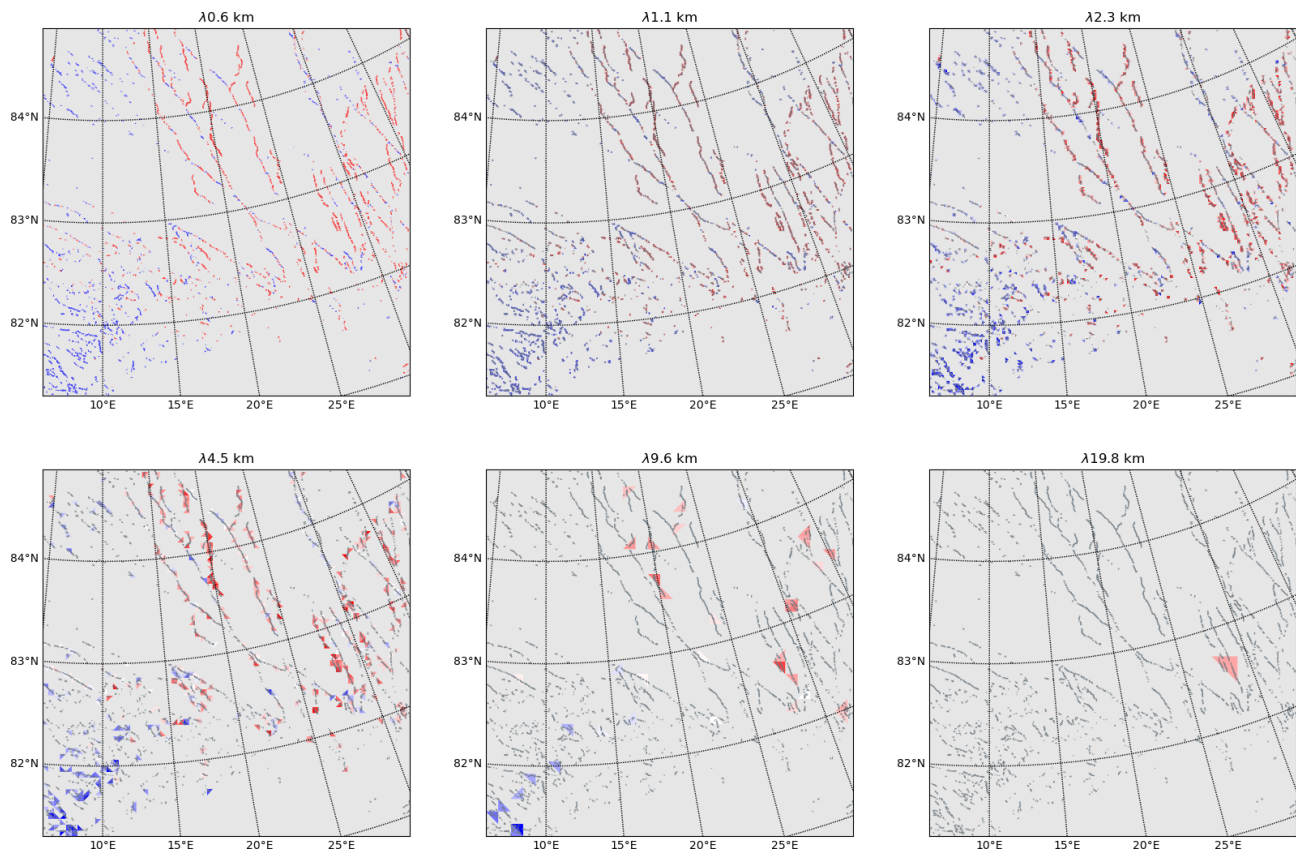
Figure 7. Example of coarse-graining of LKFF sea ice deformation for SAR image pairs for 25 January 2015. The sizes of the frames are 400 km by 400 km. The area with values below DL is shaded in gray. The coverage of the smallest triangles at λ 0.6 km is shown in all other panels with dark gray triangle outlines.

undergoing repeated deformation in the form of both divergence and convergence. Convergence and mixed deformation are localized and confined to narrow belts on the edges of predominantly diverging ice, a phenomenon observed despite changes in weather conditions and frequent alterations in sea ice drift directions (Graham et al., 2019). This finding aligns with previous studies and indicates that large fractures, where shear and shape mismatch occurred, healed slowly (Coon et al., 2007; Oikkonen et al., 2017). Recent observational studies on pressure ridges have confirmed that their keels consolidate over a period of weeks and months (Salganik et al., 2023a). The duration of sequential deformation observed in the damage parcel data can be valuable for constraining the damage–healing behavior of numerical models (Rampal et al., 2016; Damsgaard et al., 2021; Ólason et al., 2022).

Undamaged ice that did not experience any detected deformation did not move uniformly, resulting in variable distances between individual parcels (Fig. 8). Although sea ice parcel classification was based on the filtered sea ice deformation retrieval, its motion was determined using the unfiltered sea ice displacement. The density of parcels in Fig. 8 indicated undetected deformation with values below the DL.

The noise originating from artifacts in the sea ice displacement algorithm was inherently random, and any regular spatial features visible in the ice parcel density were likely a consequence of deformation. For example, in the southern part of the map, there was a continuous curve with increased parcel density (marked by "A" in Fig. 8), which pointed to real deformation. Under convergence, the relative motion is typically shorter than under divergence and more challenging to detect. As another example, the areas in the southwestern and northeastern corners of the map had sparser parcels (marked by "B" in Fig. 8), indicating divergence.

4.3 CDCs and LKFs

In contrast to the damage parcels, CDC analysis was successfully applied to the sea ice deformation calculations over the entire period from 15 January to 18 February. CDC maps (Fig. 10 top) showed evolving shapes of the CDCs, resembling ice plates seen in optical images (Erlingsson, 1988; Schulson, 2004). These shapes were obtained from daily SAR image pairs and those with shorter or longer time differences. The method was also successfully applied in the marginal ice zone (MIZ), although it fails in areas directly
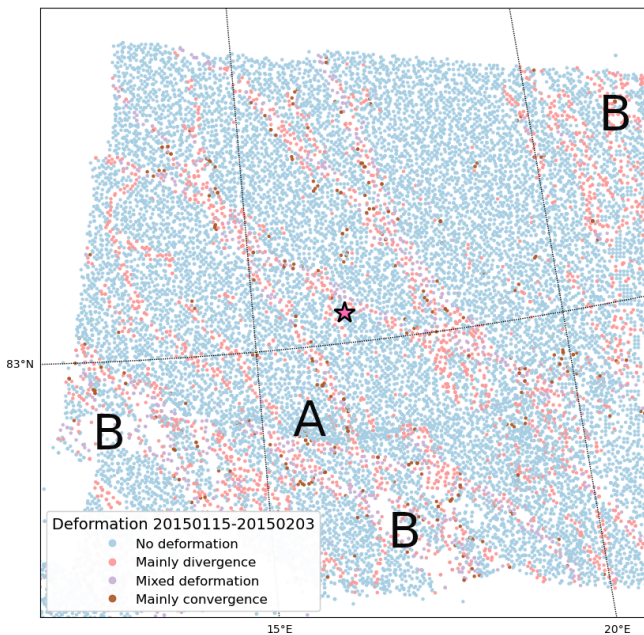
Figure 8. Damage parcel map after 19 d of sea ice drift between 15 January and 3 February 2015. Special regions of interest are marked by capital letters: A – locations with dense parcels indicating undetected convergence and B – locations with sparser parcels indicating undetected divergence. The size of the map is 120 km by 120 km. The location of RV *Lance* is represented by a pink star in the center of the map.

at the ice edge and in open water areas. The maps display a gradient in CDC size, fragmentation and roundness in the north–south direction from the pack ice towards the MIZ.

Based on the CDC maps (Fig. 9), time series of CDC statistics (Fig. 10) were calculated. The time series follow the drift of RV *Lance* to the ice edge until 22 February, after which they were extended by 10 d to account for the relocation of RV *Lance* northwards away from the MIZ (Granskog et al., 2018). In the first and last week of the time series, statistics fluctuated around values typical of the quiescent state of the pack ice. The values changed abruptly with each of the three major storms (marked by A, B and C and Fig. 10a) that passed the area (Graham et al., 2019):

– *CDC density*. The CDC density increased from low values below 5 CDCs per 100 by 100 km during quiescent periods to as high as 20 during the storms (Fig. 10a).

– *CDC area*. During the initial quiescent period, the number of CDCs was low, coinciding with a small variability in CDC area, with means just below 10 000 km^2. After the first storm in mid-January (A), the values decreased by an order of magnitude to 1000 km^2. The initial high values were never restored but increased significantly again after the relocation of RV *Lance* away from the MIZ (Fig. 10b).

– *CDC circularity*. The CDCs were generally not round, as their values were lower than the theoretical value of 1 for circular forms. Typical values were closer to 0.75, indicating more rectangular forms. There was a continuous weak increase in CDC roundness during the entire duration of the time series. The *roundness* of CDCs was typically about 2. In comparison, typical roundness values of summer sea ice floes are similar – between 1 and 4 – but with the most frequent value reported as 1.4 (Hwang and Wang, 2022) (Fig. 10c).

– *CDC complexity*. This measure of under-detected fractures exhibited the largest variability during quiescent periods, reflecting the smallest and most challenging relative motion to detect by SAR. The maps showed that fragmentation was the lowest in the MIZ, where distances between the CDCs were the largest, and relative motion was high (Figs. 9, 10d).

– *LKF fraction*. The lowest LKF fractions, close to 1 %, were recorded in mid-January and occasionally increased towards 3 % during storms. They remained relatively high (close to 2 %) in quiescent periods and after the relocation away from the MIZ. The max LKF fractions were typically above 5 % during quiescent periods but as high as 30 % during the storms. This indicates that a clear definition of CDC boundaries during the storms is difficult (Fig. 10e).

– *Distance between LKFs*. The maximal and minimal distances between LKFs estimated from CDC diameters were typically at least 5 to 10 km and at most 50 to 100 km. The highest values were found during quiescent periods and the lowest during the storms. The distance between the LKFs derived from the CDC perimeters confirmed the findings about the power law breaking, discussed in the "Results and discussion" section under "Comparison of the N-ICE2015 strain rates". The lowest distances were between 5 and 10 km, corresponding to the λ breaking point (Fig. 10f).

Despite the fierceness of the storm (B) in mid-February (Itkin et al., 2017; Graham et al., 2019), the CDC properties at the end of the time series resembled the ones at the beginning. This pointed to the resilience of the CDCs and their geometrical properties in the winter pack ice and the potential for healing. However, some properties, such as CDC area, circularity and LKF fraction, never fully recovered to the values recorded at the beginning of the time series. Itkin et al. (2017) previously demonstrated an elevated slope of the power law of the N-ICE2015 spring buoy array (April–May 2015) and hypothesized long-lasting damage to the sea ice cover caused by this extreme storm.
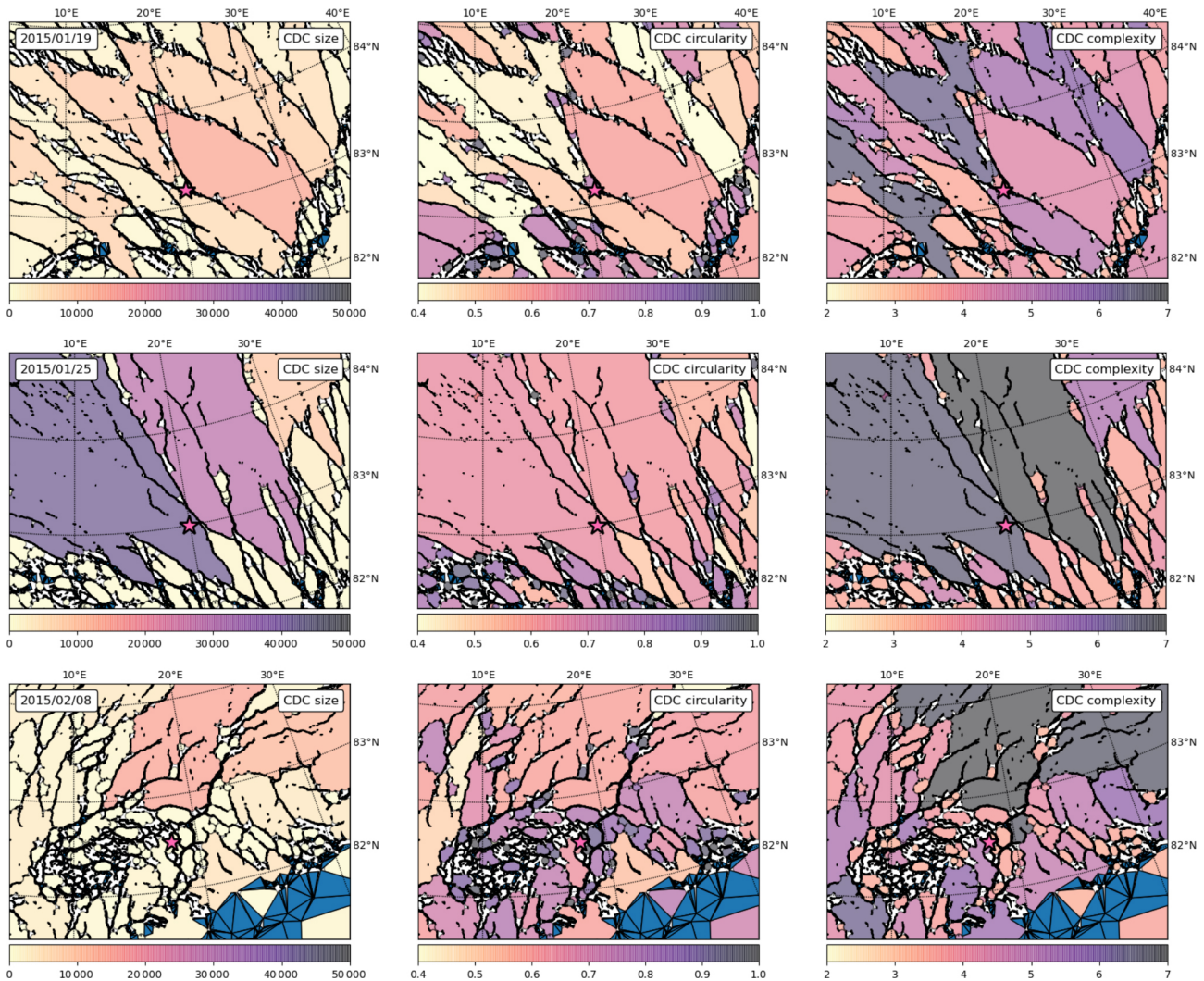
Figure 9. Examples of CDC maps with shape statistics (size, circularity and complexity) for SAR image pairs for 19 January, 25 January and 8 February 2015. Time stamps of the second image in the pair are attributed to the result. The sizes of the frames are 400 km by 300 km. The location of RV *Lance* is represented by a pink star. The distance from the ship to the MIZ decreases with time, and on 8 February, MIZ already occupied the whole southeast corner of the map.

5 Conclusions

This study has successfully demonstrated that Sentinel-1 SAR-derived sea ice deformation data can be effectively utilized at a spatial resolution of 800 m after mitigating noise generated by a sea ice displacement algorithm. This was accomplished through the application of threshold and shape filtering techniques. The accuracy of the SAR-based results was validated against data from the N-ICE2015 ship radar and buoy observations, utilizing power law properties.

Across spatial scales ranging from 600 m to 5 km, the power law slope and intercept for all three datasets (processed in a similar manner) were consistently close to 20 and −0.7, respectively. Subsequently, the strain rates were recalculated to obtain total displacements, revealing a mean total displacement of approximately 200 m at the spatial scale of 1 km.

While the power laws of all three datasets exhibited a strong correspondence below 5 km, the SAR-derived power law breaks for larger spatial scales. This discrepancy can be attributed to issues related to spatial resolution, wherein fractures smaller than LKFs are inadequately resolved, coupled with limitations in spatial extent.

The detection of SAR deformation was constrained not only by the lower limit of the spatial resolution but also by the minimum angle of triangles employed in Green's theorem (upper limit).

The damage parcels, derived from SAR-based displacements and strain rates, were effectively employed to monitor the evolution of the sea ice cover over a period of 3 weeks,
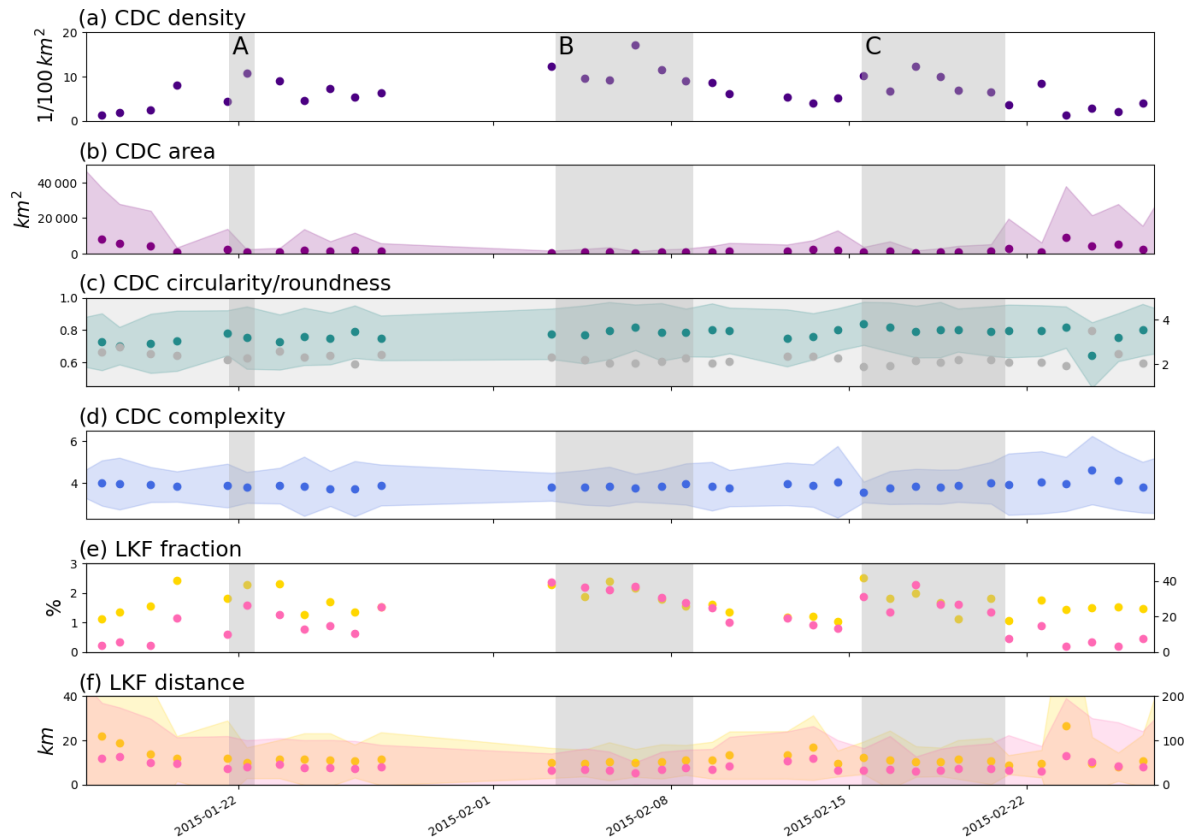
Figure 10. Time series of CDC statistics for N-ICE2015 leg 1 extended to 27 February 2015: **(a)** density, **(b)** area, **(c)** circularity in green and roundness in gray, **(d)** complexity, **(e)** min LKF fraction in yellow and max LKF fraction in pink, and **(f)** min distance between LKFs in yellow and max distance between LKFs in pink. The shading always implies 1 standard deviation from the mean. Storm periods are marked by gray shading and annotated by the capital letters A, B and C. The ship relocated away from the MIZ on 22 February.

encompassing the passage of a major storm and an 8 d data gap. The temporal stability of the ice pattern was disrupted by an extreme storm in mid-February, as reported by Graham et al. (2019), after which the tracking of damage parcels became unfeasible.

Up to 20 separate CDCs per area of 100 km by 100 km for each SAR image pair were identified based on the positions of LKFs detected through SAR-derived deformation. During quiescent periods, their typical sizes were $10\,000\,\mathrm{km}^2$, whereas they reduced to $1000\,\mathrm{km}^2$ during storms. These CDCs exhibited mainly rectangular shapes, more elongated than the sea ice floes after breakup, as reported by Hwang and Wang (2022). The fraction of the surface area covered by LKFs typically remained below 3 %, but the boundaries between CDCs and LKFs may become difficult to establish during the strongest deformation events. The distances between LKFs varied between 5–10 and 50–100 km, reflecting minimal and maximal values, respectively.

All the methods employed in this study are applicable to both the winter sea pack ice and the MIZ areas. Furthermore, the spatial resolution can be enhanced for Sentinel-1 SAR, and these methods remain adaptable to dense sea ice defor-

mation retrieval from radar or optical imagery, regardless of the data source. In the follow-up paper the method will be employed to a longer time series over the entire winter season (e.g., MOSAiC). This will allow for the analysis of processes such as "reactivation" of damage parcels after a long "relaxation time" and seasonal development of CDCs.

resentation in this paper. While Copernicus Publications makes every effort to include appropriate place names, the final responsibility lies with the authors.

Review statement. This paper was edited by Vishnu Nandan and reviewed by Stephen Howell and Andrew Mahoney.

References

Bouillon, S. and Rampal, P.: On producing sea ice deformation data sets from SAR-derived sea ice motion, The Cryosphere, 9, 663–673, https://doi.org/10.5194/tc-9-663-2015, 2015.

Bushuk, M., Msadek, R., Winton, M., Vecchi, G. A., Gudgel, R., Rosati, A., and Yang, X.: Skillful regional prediction of Arctic sea ice on seasonal timescales, Geophys. Res. Lett., 44, 4953–4964, https://doi.org/10.1002/2017GL073155, 2017.

Clemens-Sewall, D., Polashenski, C., Raphael, I., Perovich, D., and Fons, S.: High-Resolution Repeat Topography of Drifting Ice Floes in the Arctic Ocean from Terrestrial Laser Scanning Collected on the Multidisciplinary drifting Observatory for the Study of Arctic Climate Expedition, Arctic Data Center [data set], https://doi.org/10.18739/A26688K9D, 2022.

CloudFerro: Sentinel-1 L1 GRD, https://creodias.eu/, last access: 1 May 2023.

Coon, M., Kwok, R., Levy, G., Pruis, M., Schreyer, H., and Sulsky, D.: Arctic Ice Dynamics Joint Experiment (AIDJEX) assumptions revisited and found inadequate, J. Geophys. Res.-Oceans, 112, C11S90, https://doi.org/10.1029/2005JC003393, 2007.

Copernicus Sentinel data: https://creodias.eu/ (last access: 1 April 2023), 2023.

Damsgaard, A., Sergienko, O., and Adcroft, A.: The Effects of Ice Floe-Floe Interactions on Pressure Ridging in Sea Ice, J. Adv. Model. Earth Sy., 13, e2020MS002336, https://doi.org/10.1029/2020MS002336, 2021.

Dansereau, V., Démery, V., Berthier, E., Weiss, J., and Ponson, L.: Collective Damage Growth Controls Fault Orientation in Quasibrittle Compressive Failure, Phys. Rev. Lett., 122, 085501, https://doi.org/10.1103/PhysRevLett.122.085501, 2019.

Erlingsson, B.: Two-Dimensional Deformation Patterns in Sea Ice, J. Glaciol., 34, 301–308, https://doi.org/10.3189/S0022143000007061, 1988.

Farrell, S. L., Duncan, K., Buckley, E. M., Richter-Menge, J., and Li, R.: Mapping Sea Ice Surface Topography in High Fidelity With ICESat-2, Geophys. Res. Lett., 47, e2020GL090708, https://doi.org/10.1029/2020GL090708, 2020.

Girard, L., Bouillon, S., Weiss, J., Amitrano, D., Fichefet, T., and Legat, V.: A new modeling framework for sea-ice mechanics based on elasto-brittle rheology, Ann. Glaciol., 52, 123–132, 2011.

Graham, R. M., Itkin, P., Meyer, A., Sundfjord, A., Spreen, G., Smedsrud, L. H., Liston, G. E., Cheng, B., Cohen, L., Divine, D., Fer, I., Fransson, A., Gerland, S., Haapala, J., Hudson, S. R., Johansson, A. M., King, J., Merkouriadi, I., Peterson, A. K., Provost, C., Randelhoff, A., Rinke, A., Rösel, A., Sennéchael, N., Walden, V. P., Duarte, P., Assmy, P., Steen, H., and Granskog, M. A.: Winter storms accelerate the demise of sea ice in the Atlantic sector of the Arctic Ocean, Sci. Rep., 9, 9222, https://doi.org/10.1038/s41598-019-45574-5, 2019.

Granskog, M. A., Fer, I., Rinke, A., and Steen, H.: Atmosphere-Ice-Ocean-Ecosystem Processes in a Thinner Arctic Sea Ice Regime: The Norwegian Young Sea ICE (N-ICE2015) Expedition, J. Geophys. Res.-Oceans, 123, 1586–1594, https://doi.org/10.1002/2017JC013328, 2018.

Guo, W., Itkin, P., Lohse, J., Johansson, M., and Doulgeris, A. P.: Cross-platform classification of level and deformed sea ice considering per-class incident angle dependency of backscatter intensity, The Cryosphere, 16, 237–257, https://doi.org/10.5194/tc-16-237-2022, 2022.

Guo, W., Itkin, P., Singha, S., Doulgeris, A. P., Johansson, M., and Spreen, G.: Sea ice classification of TerraSAR-X ScanSAR images for the MOSAiC expedition incorporating per-class incidence angle dependency of image texture, The Cryosphere, 17, 1279–1297, https://doi.org/10.5194/tc-17-1279-2023, 2023.

Haapala, J., Oikkonen, A., Gierisch, A., Itkin, P., Nicolaus, M., Spreen, G., Wang, C., Karvonen, J., and Lensu, M.: N-ICE2015 ship radar images, Norwegian Polar Institute [data set], https://doi.org/10.21334/npolar.2017.6441ca81, 2017.

Heorton, H. D. B. S., Feltham, D. L., and Tsamados, M.: Stress and deformation characteristics of sea ice in a high-resolution, anisotropic sea ice model, Philos. T. Roy. Soc. A, 376, 20170349, https://doi.org/10.1098/rsta.2017.0349, 2018.

Hibler, W. D.: A Dynamic Thermodynamic Sea Ice Model, J. Phys. Oceanogr., 9, 815–846, https://doi.org/10.1175/1520-0485(1979)009<0815:ADTSIM>2.0.CO;2, 1979.

Hollands, T. and Dierking, W.: Performance of a multiscale correlation algorithm for the estimation of sea-ice drift from SAR images: initial results, Ann. Glaciol., 52, 311–317, https://doi.org/10.3189/172756411795931462, 2011.

Horvath, S., Boisvert, L., Parker, C., Webster, M., Taylor, P., Boeke, R., Fons, S., and Stewart, J. S.: Database of daily Lagrangian Arctic sea ice parcel drift tracks with coincident ice and atmospheric conditions, Sci. Data, 10, 73, https://doi.org/10.1038/s41597-023-01987-6, 2023.

Howell, S. E. L., Brady, M., and Komarov, A. S.: Generating large-scale sea ice motion from Sentinel-1 and the RADARSAT Constellation Mission using the Environment and Climate Change

Canada automated sea ice tracking system, The Cryosphere, 16, 1125–1139, https://doi.org/10.5194/tc-16-1125-2022, 2022.

Hunke, E. C. and Dukowicz, J. K.: An Elastic–Viscous–Plastic Model for Sea Ice Dynamics, J. Phys. Oceanogr., 27, 1849–1867, https://doi.org/10.1175/1520-0485(1997)027<1849:AEVPMF>2.0.CO;2, 1997.

Hutchings, J. K. and Hibler III, W. D.: Small-scale sea ice deformation in the Beaufort Sea seasonal ice zone, J. Geophys. Res.-Oceans, 113, C08032, https://doi.org/10.1029/2006JC003971, 2008.

Hutchings, J. K., Roberts, A., Geiger, C. A., and Richter-Menge, J.: Spatial and temporal characterization of sea-ice deformation, Ann. Glaciol., 52, 360–368, https://doi.org/10.3189/172756411795931769, 2011.

Hutchings, J. K., Heil, P., Steer, A., and Hibler III, W. D.: Subsynoptic scale spatial variability of sea ice deformation in the western Weddell Sea during early summer, J. Geophys. Res.-Oceans, 117, C01002, https://doi.org/10.1029/2011JC006961, 2012.

Hutter, N., Bouchat, A., Dupont, F., Dukhovskoy, D., Koldunov, N., Lee, Y. J., Lemieux, J.-F., Lique, C., Losch, M., Maslowski, W., Myers, P. G., Ólason, E., Rampal, P., Rasmussen, T., Talandier, C., Tremblay, B., and Wang, Q.: Sea Ice Rheology Experiment (SIREx): 2. Evaluating Linear Kinematic Features in High-Resolution Sea Ice Simulations, J. Geophys. Res.-Oceans, 127, e2021JC017666, https://doi.org/10.1029/2021JC017666, 2022.

Hwang, B. and Wang, Y.: Multi-scale satellite observations of Arctic sea ice: new insight into the life cycle of the floe size distribution, Philos. T. Roy. Soc. A, 380, 20210259, https://doi.org/10.1098/rsta.2021.0259, 2022.

Itkin, P.: sid – Sea Ice Deformation from imaging remote sensing data, Zenodo [code], https://doi.org/10.5281/zenodo.14543427, 2024.

Itkin, P., Spreen, G., Cheng, B., Doble, M., Gerland, S., Granskog, M. A., Haapala, J., Hudson, S. R., Kaleschke, L., Nicolaus, M., Pavlov, A., Shestov, A., Steen, H., Wilkinson, J., and Helgeland, C.: N-ICE2015 buoy data , Norwegian Polar Institute [data set], 10, https://doi.org/10.21334/npolar.2015.6ed9a8ca, 2015.

Itkin, P., Spreen, G., Cheng, B., Doble, M., Girard-Ardhuin, F., Haapala, J., Hughes, N., Kaleschke, L., Nicolaus, M., and Wilkinson, J.: Thin ice and storms: Sea ice deformation from buoy arrays deployed during N-ICE2015, J. Geophys. Res.-Oceans, 122, 4661–4674, https://doi.org/10.1002/2016JC012403, 2017.

Itkin, P., Spreen, G., Hvidegaard, S. M., Skourup, H., Wilkinson, J., Gerland, S., and Granskog, M. A.: Contribution of Deformation to Sea Ice Mass Balance: A Case Study From an N-ICE2015 Storm, Geophys. Res. Lett., 45, 789–796, https://doi.org/10.1002/2017GL076056, 2018.

Karvonen, J.: Virtual radar ice buoys – a method for measuring fine-scale sea ice drift, The Cryosphere, 10, 29–42, https://doi.org/10.5194/tc-10-29-2016, 2016.

Komarov, A. S. and Barber, D. G.: Sea Ice Motion Tracking From Sequential Dual-Polarization RADARSAT-2 Images, IEEE T. Geosci. Remote, 52, 121–136, https://doi.org/10.1109/TGRS.2012.2236845, 2014.

Korosov, A. A. and Rampal, P.: A Combination of Feature Tracking and Pattern Matching with Optimal Parametrization for Sea Ice Drift Retrieval from SAR Data, Remote Sens., 9, 3, https://doi.org/10.3390/rs9030258, 2017.

Kwok, R.: The RADARSAT Geophysical Processor System, Springer Berlin Heidelberg, Berlin, Heidelberg, 235–257, ISBN 978-3-642-60282-5, https://doi.org/10.1007/978-3-642-60282-5_11, 1998.

Kwok, R.: Deformation of the Arctic Ocean Sea Ice Cover between November 1996 and April 1997: A Qualitative Survey, in: IUTAM Symposium on Scaling Laws in Ice Mechanics and Ice Dynamics, edited by: Dempsey, J. P. and Shen, H. H., Springer Netherlands, Dordrecht, 315–322, ISBN 978-94-015-9735-7, 2001.

Kwok, R. and Cunningham, G. F.: Variability of Arctic sea ice thickness and volume from CryoSat-2, Philos. T. Roy. Soc. A, 373, 20140157, https://doi.org/10.1098/rsta.2014.0157, 2015.

Landy, J. C., Petty, A. A., Tsamados, M., and Stroeve, J. C.: Sea Ice Roughness Overlooked as a Key Source of Uncertainty in CryoSat-2 Ice Freeboard Retrievals, J. Geophys. Res.-Oceans, 125, e2019JC015820, https://doi.org/10.1029/2019JC015820, 2020.

Lindsay, R. W. and Stern, H. L.: The RADARSAT Geophysical Processor System: Quality of Sea Ice Trajectory and Deformation Estimates, J. Atmos. Ocean. Technol., 20, 1333–1347, https://api.semanticscholar.org/CorpusID:29184923 (last access: 1 September 2024), 2003.

Liston, G. E., Itkin, P., Stroeve, J., Tschudi, M., Stewart, J. S., Pedersen, S. H., Reinking, A. K., and Elder, K.: A lagrangian snow-evolution system for sea-ice applications (SnowModel-LG): part I – model description, J. Geophys. Res.-Oceans, 125, e2019JC015913, https://doi.org/10.1029/2019JC015913, 2020.

Lohse, J., Doulgeris, A. P., and Dierking, W.: Mapping sea-ice types from Sentinel-1 considering the surface-type dependent effect of incidence angle, Ann. Glaciol., 61, 260–270, https://doi.org/10.1017/aog.2020.45, 2020.

Marsan, D., Stern, H., Lindsay, R., and Weiss, J.: Scale Dependence and Localization of the Deformation of Arctic Sea Ice, Phys. Rev. Lett., 93, 178501, https://doi.org/10.1103/PhysRevLett.93.178501, 2004.

Meredith, M., Sommerkorn, M., Cassotta, S., Derksen, C., Ekaykin, A., Hollowed, A., Kofinas, G., Mackintosh, A., Melbourne-Thomas, J., Muelbert, M. M. C., Ottersen, G., Pritchard, H., and Schuur, E. A. G.: Polar Regions, IPCC Special Report on the Ocean and Cryosphere in a Changing Climate, 203–320, https://doi.org/10.1017/9781009157964.005, 2019.

Nicolaus, M., Perovich, D. K., Spreen, G., Granskog, M. A., von Albedyll, L., Angelopoulos, M., Anhaus, P., Arndt, S., Belter, H. J., Bessonov, V., Birnbaum, G., Brauchle, J., Calmer, R., Cardellach, E., Cheng, B., Clemens-Sewall, D., Dadic, R., Damm, E., de Boer, G., Demir, O., Dethloff, K., Divine, D. V., Fong, A. A., Fons, S., Frey, M. M., Fuchs, N., Gabarró, C., Gerland, S., Goessling, H. F., Gradinger, R., Haapala, J., Haas, C., Hamilton, J., Hannula, H.-R., Hendricks, S., Herber, A., Heuzé, C., Hoppmann, M., Høyland, K. V., Huntemann, M., Hutchings, J. K., Hwang, B., Itkin, P., Jacobi, H.-W., Jaggi, M., Jutila, A., Kaleschke, L., Katlein, C., Kolabutin, N., Krampe, D., Kristensen, S. S., Krumpen, T., Kurtz, N., Lampert, A., Lange, B. A., Lei, R., Light, B., Linhardt, F., Liston, G. E., Loose, B., Macfarlane, A. R., Mahmud, M., Matero, I. O., Maus, S., Morgenstern, A., Naderpour, R., Nandan, V., Niubom, A., Oggier, M., Oppelt, N., Pätzold, F., Perron, C., Petrovsky, T., Pirazzini, R., Polashenski, C., Rabe, B., Raphael, I. A., Regnery, J., Rex,

M., Ricker, R., Riemann-Campe, K., Rinke, A., Rohde, J., Salganik, E., Scharien, R. K., Schiller, M., Schneebeli, M., Semmling, M., Shimanchuk, E., Shupe, M. D., Smith, M. M., Smolyanitsky, V., Sokolov, V., Stanton, T., Stroeve, J., Thielke, L., Timofeeva, A., Tonboe, R. T., Tavri, A., Tsamados, M., Wagner, D. N., Watkins, D., Webster, M., and Wendisch, M.: Overview of the MOSAiC expedition: snow and sea ice, Elementa, 10, 000046, https://doi.org/10.1525/elementa.2021.000046, 2022.

Oikkonen, A., Haapala, J., Lensu, M., and Karvonen, J.: Sea ice drift and deformation in the coastal boundary zone, Geophys. Res. Lett., 43, 10303–10310, https://doi.org/10.1002/2016GL069632, 2016.

Oikkonen, A., Haapala, J., Lensu, M., Karvonen, J., and Itkin, P.: Small-scale sea ice deformation during N-ICE2015: From compact pack ice to marginal ice zone, J. Geophys. Res.-Oceans, 122, 5105–5120, https://doi.org/10.1002/2016JC012387, 2017.

Olason, E. and Notz, D.: Drivers of variability in Arctic sea-ice drift speed, J. Geophys. Res.-Oceans, 119, 5755–5775, https://doi.org/10.1002/2014JC009897, 2014.

Ólason, E., Boutin, G., Korosov, A., Rampal, P., Williams, T., Kimmritz, M., Dansereau, V., and Samaké, A.: A New Brittle Rheology and Numerical Framework for Large-Scale Sea-Ice Models, J. Adv. Model. Earth Sy., 14, e2021MS002685, https://doi.org/10.1029/2021MS002685, 2022.

Parno, J., Polashenski, C., Parno, M., Nelsen, P., Mahoney, A., and Song, A.: Observations of Stress-Strain in Drifting Sea Ice at Floe Scale, J. Geophys. Res.-Oceans, 127, e2021JC017761, https://doi.org/10.1029/2021JC017761, 2022.

Rampal, P., Weiss, J., and Marsan, D.: Positive trend in the mean speed and deformation rate of Arctic sea ice, 1979–2007, J. Geophys. Res.-Oceans, 114, C05013, https://doi.org/10.1029/2008JC005066, 2009.

Rampal, P., Bouillon, S., Ólason, E., and Morlighem, M.: neXtSIM: a new Lagrangian sea ice model, The Cryosphere, 10, 1055–1073, https://doi.org/10.5194/tc-10-1055-2016, 2016.

Rampal, P., Dansereau, V., Olason, E., Bouillon, S., Williams, T., Korosov, A., and Samaké, A.: On the multi-fractal scaling properties of sea ice deformation, The Cryosphere, 13, 2457–2474, https://doi.org/10.5194/tc-13-2457-2019, 2019.

Ricker, R., Hendricks, S., Kaleschke, L., Tian-Kunze, X., King, J., and Haas, C.: A weekly Arctic sea-ice thickness data record from merged CryoSat-2 and SMOS satellite data, The Cryosphere, 11, 1607–1623, https://doi.org/10.5194/tc-11-1607-2017, 2017.

Ringeisen, D., Hutter, N., and von Albedyll, L.: Deformation lines in Arctic sea ice: intersection angle distribution and mechanical properties, The Cryosphere, 17, 4047–4061, https://doi.org/10.5194/tc-17-4047-2023, 2023.

Rösel, A., Itkin, P., King, J., Divine, D., Wang, C., Granskog, M. A., Krumpen, T., and Gerland, S.: Thin sea ice, thick snow, and widespread negative freeboard observed during N-ICE2015 north of Svalbard, J. Geophys. Res.-Oceans, 123, 1156–1176, https://doi.org/10.1002/2017JC012865, 2018.

Salganik, E., Lange, B. A., Itkin, P., Divine, D., Katlein, C., Nicolaus, M., Hoppmann, M., Neckel, N., Ricker, R., Høyland, K. V., and Granskog, M. A.: Different mechanisms of Arctic first-year sea-ice ridge consolidation observed during the MOSAiC expedition, Elementa, 11, 00008, https://doi.org/10.1525/elementa.2023.00008, 2023a.

Salganik, E., Lange, B. A., Katlein, C., Matero, I., Anhaus, P., Muilwijk, M., Høyland, K. V., and Granskog, M. A.: Observations of preferential summer melt of Arctic sea-ice ridge keels from repeated multibeam sonar surveys, The Cryosphere, 17, 4873–4887, https://doi.org/10.5194/tc-17-4873-2023, 2023b.

Schulson, E. M.: Compressive shear faults within arctic sea ice: Fracture on scales large and small, J. Geophys. Res.-Oceans, 109, C07016, https://doi.org/10.1029/2003JC002108, 2004.

Tian, T., Yang, S., Karami, M. P., Massonnet, F., Kruschke, T., and Koenigk, T.: Benefits of sea ice initialization for the interannual-to-decadal climate prediction skill in the Arctic in EC-Earth3, Geosci. Model Dev., 14, 4283–4305, https://doi.org/10.5194/gmd-14-4283-2021, 2021.

von Albedyll, L., Haas, C., and Dierking, W.: Linking sea ice deformation to ice thickness redistribution using high-resolution satellite and airborne observations, The Cryosphere, 15, 2167–2186, https://doi.org/10.5194/tc-15-2167-2021, 2021.

von Albedyll, L., Hendricks, S., Grodofzig, R., Krumpen, T., Arndt, S., Belter, H. J., Birnbaum, G., Cheng, B., Hoppmann, M., Hutchings, J., Itkin, P., Lei, R., Nicolaus, M., Ricker, R., Rohde, J., Suhrhoff, M., Timofeeva, A., Watkins, D., Webster, M., and Haas, C.: Thermodynamic and dynamic contributions to seasonal Arctic sea ice thickness distributions from airborne observations, Elementa, 10, 00074, https://doi.org/10.1525/elementa.2021.00074, 2022.

Weiss, J.: Exploring the "solid turbulence" of sea ice dynamics down to unprecedented small scales, J. Geophys. Res.-Oceans, 122, 6071–6075, https://doi.org/10.1002/2017JC013236, 2017.

Wernecke, A. and Kaleschke, L.: Lead detection in Arctic sea ice from CryoSat-2: quality assessment, lead area fraction and width distribution, The Cryosphere, 9, 1955–1968, https://doi.org/10.5194/tc-9-1955-2015, 2015.

Zakhvatkina, N., Smirnov, V., and Bychkova, I.: Satellite SAR Data-based Sea Ice Classification: An Overview, Geosciences, 9, 152, https://doi.org/10.3390/geosciences9040152, 2019.

Zygmuntowska, M., Rampal, P., Ivanova, N., and Smedsrud, L. H.: Uncertainties in Arctic sea ice thickness and volume: new estimates and implications for trends, The Cryosphere, 8, 705–720, https://doi.org/10.5194/tc-8-705-2014, 2014.